Structural Studies of Amphiphilic 4-Helix Bundle Peptides Incorporating Designed Extended Chromophores for Nonlinear Optical Biomolecular Materials

Joseph Strzalka,[†] Ting Xu,[†] Andrey Tronin,[†] Sophia P. Wu,[†] Ivan Miloradovic,[†] Ivan Kuzmenko,[‡] Thomas Gog,[‡] Michael J. Therien,[†] and J. Kent Blasie*,[†]

Department of Chemistry, University of Pennsylvania, 231 South 34th Street, Philadelphia, Pennsylvania 19104, and Complex Materials Consortium, Advanced Photon Source, Argonne National Laboratory, Argonne, Illinois 60439

ABSTRACT

Extended conjugated chromophores containing (porphinato)zinc components that exhibit large optical polarizabilities and hyperpolarizabiliites are incorporated into amphiphilic 4-helix bundle peptides via specific axial histidyl ligation of the metal. The bundle's designed amphiphilicity enables vectorial orientation of the chromophore/peptide complex in macroscopic monolayer ensembles. The 4-helix bundle structure is maintained upon incorporation of two different chromophores at stoichiometries of 1–2 per bundle. The axial ligation site appears to effectively control the position of the chromophore along the length of the bundle.

In an accompanying paper,[1] we describe the use of axial histidyl ligation coordination chemistry to direct the incorporation of designed extended multipigment ensembles that feature a (porphinato)zinc component into amphiphilic 4-helix bundles for nonlinear optical biomolecular material applications.[2] The incorporation of 5,5′-bis[(10,20-di-((4-carboxymethyleneoxy)phenyl)porphinato)zinc(II)]butadiyne (PZnE-EPZn, previously referred to as "Zn33Zn"[3]) and ruthenium(II) [5-(4′-ethynyl-(2,2′;6′,2′ ′-terpyridinyl))-10,20-bis(2′,6′-bis(3,3-dimethyl-1-butyloxy)phenyl)porphinato]zinc-(II)-(2,2′;6′,2′′-terpyridine)[2+] (Ru-PZn[2+]),[4,5] which feature ethyne-based chromophore-to-chromophore connectivity that drives substantial electronic coupling between their respective component pigments,[6−14] into the designed amphiphilic 4-helix bundle peptides allows for the both vectorial orientation of these supermolecular, electro-optically active species in macroscopic ensembles and the control over chromophore−chromophore interactions.

Here we describe structural studies of one of these peptides, the prototype H6H20 AP0 possessing two ligation sites along the length of the hydrophilic domain of the 4-helix bundle,[2] and its variants F6H20 and H6F20 each possessing only one of the two ligation sites, with two different extended conjugated chromophores: PZnE-EPZn, a butadiyne-bridged bis[(porphinato)zinc] complex that possesses diminished

potentiometric and optical band-gaps relative to simple monomeric (porphinato)metal compounds, and Ru-PZn[2+], a supermolecular nonlinear optical chromophore that features optimal alignment and substantial coupling between its component (porphinato)metal and (terpyridyl)metal charge-transfer transition dipoles. The chemical structures of these two cofactors, taken from the accompanying paper,[1] are shown below. These structural studies employ synchrotron radiation-based X-ray reflectivity, grazing-incidence X-ray diffraction, and polarized optical absorption-emission spectroscopy on vectorially oriented single monolayers of the peptide−chromophore complexes. The *apo* form of the AP0 peptides, that is, in the absence of a chromophoric cofactor, can be spread in Langmuir monolayers at the air−water interface from methanol solution. However, in order to facilitate direct comparisons between the *apo* form of the peptides and their *holo* forms, that is, with specifically bound cofactors at particular cofactor−peptide mole ratios, both the pure peptides and their corresponding cofactor/peptide complexes were spread from otherwise identical detergent solutions to form the Langmuir monolayers. Minimal amounts of the detergent *n*-octyl *β*-D-glucopyranoside (OG) were employed, namely, 0.9% as required to solubilize the amphiphilic 4-helix bundle peptides, with resulting detergent/peptide mole ratios of approximately 300:1. The pressure−area isotherms for the *apo* form of H6H20 AP0 and its *holo* form with the PZnE-EPZn cofactor at a cofactor/peptide mole ratio of 1/4-helix bundle are shown in Figure 1. The isotherm

* Corresponding author. E-mail: jkblasie@sas.upenn.edu.
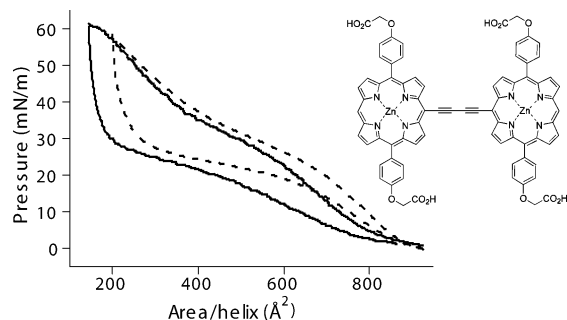† University of Pennsylvania.
‡ Argonne National Laboratory.

Figure 1. Pressure−area isotherms for Langmuir monolayers of the H6H20 AP0 peptide for the *apo* form (dotted line) and the *holo* form (solid line) with the PZnE-EPZn cofactor (inset) at one cofactor/4-helix bundle. A large hysteresis in the compression−expansion cycle for both forms is readily apparent.

for the *apo* form is typical of that for the peptide spread from methanol, first exhibiting finite pressure upon compression at an area/helix of ∼900 Å². Upon further compression, the pressure rises relatively steeply to ∼30 mN/m at an area/helix of ∼700 Å², then less steeply to a pressure of ∼40 mN/m at an area of ∼400 Å², before rising more steeply again to the maximal high pressure of ∼60 mN/m for areas/helix approaching ∼200 Å². A large hysteresis is evident on subsequent expansion and the isotherm shows reasonable reproducibility upon a subsequent cycle of compression−expansion. Given the ∼63 Å length of the helices (i.e., 42 residues at 1.5 Å/residue) with a diameter of ∼10 Å, the isotherm for the *apo*-AP0 is consistent with the helices lying in the plane of the interface at surface pressures of 20−30 mN/m and lower, and roughly perpendicular to the plane at the higher surface pressures of 50−60 mN/m. The isotherm for the *holo* form of the H6H20 AP0 is similar to that of the *apo* form but shifted slightly by ∼50 Å² toward smaller areas/helix. A large hysteresis is also evident for the *holo* form on subsequent expansion and the isotherm again shows reasonable reproducibility upon a subsequent cycle of compression−expansion. These large hysteresis effects for both the *apo* and *holo* forms of AP0 suggest that the 4-helix bundles formed at the interface at higher surface pressures, as shown below via grazing-incidence X-ray diffraction, are indeed stable. Similar results (not shown here) were obtained for the F6H20 and H6F20 variants of the AP0 peptide for both *apo* and *holo* forms with the PZnE-EPZn cofactor, the latter at the same cofactor/peptide mole ratio as for the H6H20 AP0 peptide, namely, 1 cofactor/4-helix bundle. In addition, the incorporation of the PZnE-EPZn cofactor's monomeric building block (10,20-di-((4-carboxymethyleneoxy)phenyl)-porphinato)zinc(II) (DPP-Zn), at the same cofactor/peptide mole ratio resulted in an isotherm virtually identical to that observed for PZnE-EPZn. Similar results (again, not shown here) were also obtained for the H6F20 and H6H20 variants of the AP0 peptide with the Ru-PZn²⁺ cofactor at 1 cofactor/4-helix bundle, noting that this cofactor does not bind to the dimer (or dihelical) form of the F6H20 variant.

Normalized X-ray reflectivity data, $R(q_z)/R_F(q_z)$, were collected from Langmuir monolayers of both the *apo* and *holo* forms of the AP0 peptides H6H20, H6F20, and F6H20
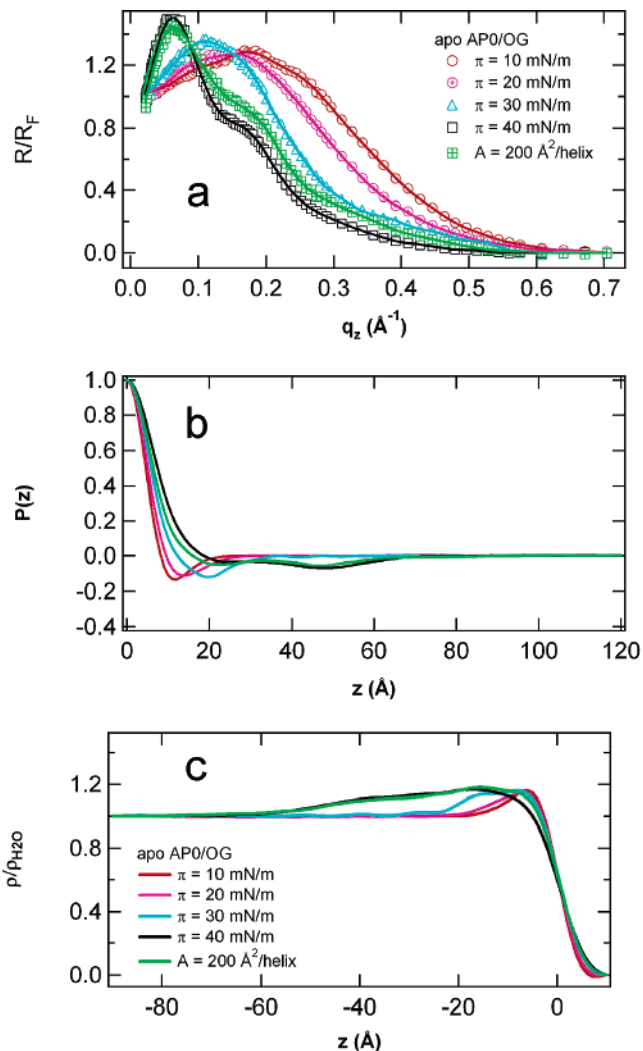

Figure 2. Fresnel-normalized X-ray reflectivity data (upper), and the corresponding autocorrelation of the gradient electron density profiles (middle) and absolute electron density profiles themselves (lower) derived from these data, for Langmuir monolayers of the *apo* form of the H6H20 variant of the AP0 peptide as a function of the applied surface pressure. At the higher pressures, data were also collected at constant area, as opposed to constant pressure. The minimum in these (and subsequent) autocorrelation functions (b) in the region 40 Å < z < 60 Å at the higher surface pressures is a direct measure of the length of the peptide bundle projected onto the monolayer profile z axis, and its depth (and width) are directly (and inversely) related to the sharpness of the interface between the hydrophilic domain of the peptide and the pure aqueous subphase beneath the peptide monolayer.

with the PZnE-EPZn cofactor at a cofactor/peptide mole ratio of 1/4-helix bundle, and for the H6H20 variant with the Ru-PZn²⁺ cofactor also at a cofactor/peptide mole ratio of 1/4-helix bundle, as a function of surface pressure. These data were analyzed via the so-called box-refinement procedure to provide, with no a priori assumptions, both the autocorrelation function of the gradient electron density profile for the monolayer and the electron density profile itself. Both the data collection and analysis procedures have been described previously in detail and will not be repeated here.[2,15,16]

To facilitate the comparison of the resulting profile structures of the monolayers of the *apo* and *holo* forms of
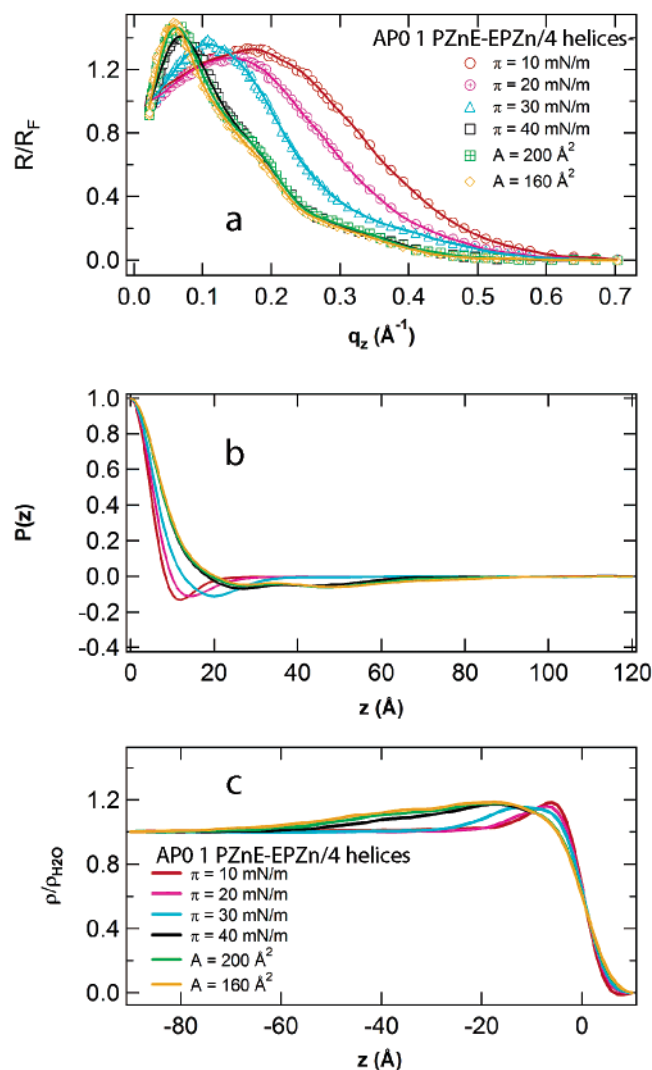
Figure 3. Fresnel-normalized X-ray reflectivity data (a), and the corresponding autocorrelation of the gradient electron density profiles (b) and absolute electron density profiles themselves (c) derived from these data, for Langmuir monolayers of the *holo* form of H6H20 AP0 with the PZnE-EPZn cofactor at one cofactor/4-helix bundle as a function of the applied surface pressure. At the higher pressures, data were also collected at constant area, as opposed to constant pressure.

the AP0 peptides investigated, we first consider the *apo* forms of the variants H6H20, F6H20, and H6F20, with reference to Figure 2. At the lower surface pressures of 10–20 mN/m, the monolayer electron density profiles for the *apo* forms of H6H20 AP0 are consistent with the long axis of each helix in the dihelix lying in the plane of the interface resulting in a single maximum in the monolayer electron density profile ∼10 Å in width, corresponding to the diameter of an α helix, located at the interface. At slightly higher surface pressures of ∼30 mN/m, the plane of the dihelix rotates to perpendicular to the plane of the interface, but with the long axis of the helices remaining parallel to the interface, resulting in the electron density profile of the monolayer exhibiting a single broader maximum at the interface ∼20 Å in width, thereby accommodating the two α-helices of the dihelix. Finally, at surface pressures of 40 mN/m and above, the electron density profile of the monolayer of the

apo form of H6H20 AP0 extends about 60 Å from the interface into the subphase, being relatively uniform over the −45 to −5 Å region of the profile with the exception of a slight maximum at $z \approx -20$ Å. Considering the nature of the profiles for the monolayer at the lower pressures below 40 mN/m, this would be consistent with the long axis of the helices for a major fraction of the peptide in the monolayer, namely, about 95%, having become oriented perpendicular to the interface upon the pressure increase from 10 mN/m to 40 mN/m, with a minor fraction of the helices, namely, ∼5%, still lying in the plane of the interface. Thus, the monolayer electron density profile at ∼40 mN/m and above is well-represented quantitatively by the weighted incoherent sum of the electron density profile for the H6H20 AP0 helices oriented perpendicular to the monolayer plane and the profile for the AP0 helices oriented parallel to the monolayer plane, for example, the monolayer profile at ∼10 mN/m, the weighting factors given by the fractional areas occupied for each orientation in the monolayer plane. In this incoherent superposition, the minor fraction of helices lying parallel to the monolayer plane must be positioned in the monolayer profile at the air−water interface, namely, at the junction between the hydrophilic and hydrophobic domains of the helices lying perpendicular to the interface, namely, centered at $z \approx -20$ Å. Properly accounting for this superposition results in a profile for the H6H20 AP0 helices being relatively uniform over their ∼60 Å length perpendicular to the monolayer plane. Overall, each helix of AP0 has 42 residues, which provides a length of ∼63 Å for a perfect straight α-helix at 1.5 Å/residue along the long axis. For the H6H20 variant, this behavior is entirely similar for monolayers spread from either methanol or detergent solution, and is effectively the norm. For the F6H20 and H6F20 variants of AP0, it appears to be more difficult to achieve such a large fraction of helices oriented perpendicular to the interface at higher surface pressures when spread from detergent solution, based on the analysis of their respective electron density profiles as described above. This behavior complicates any comparison of the *apo* and *holo* forms, and such comparisons of the electron density profiles will therefore be presented below only for those cases in which >90% of the helices were oriented perpendicular to the interface for both forms. However, as directly relevant to the polarized spectroscopy results to be reported later on in the paper for the PZnE-EPZn cofactor, we note the following. In contrast to H6H20 AP0 where the fraction of helices oriented perpendicular to the interface at the higher surface pressures can routinely attain ∼95%, the norm for this fraction decreases substantially to 70−80% for the *holo* form of F6H20 and to 60−70% for the *holo* form of H6F20. We have no further explanation for this difference noted except that the overall hydrophobicity of the F6H20 and H6F20 variants of the AP0 amphiphilic peptide is noticeably greater (e.g., as based on their respective detergent solubilization) than for the H6H20 form, a direct result of the single H → F mutation in their sequence.

For the PZnE-EPZn cofactor and H6H20 AP0, the electron density profiles for the *apo* and the *holo* forms, at a
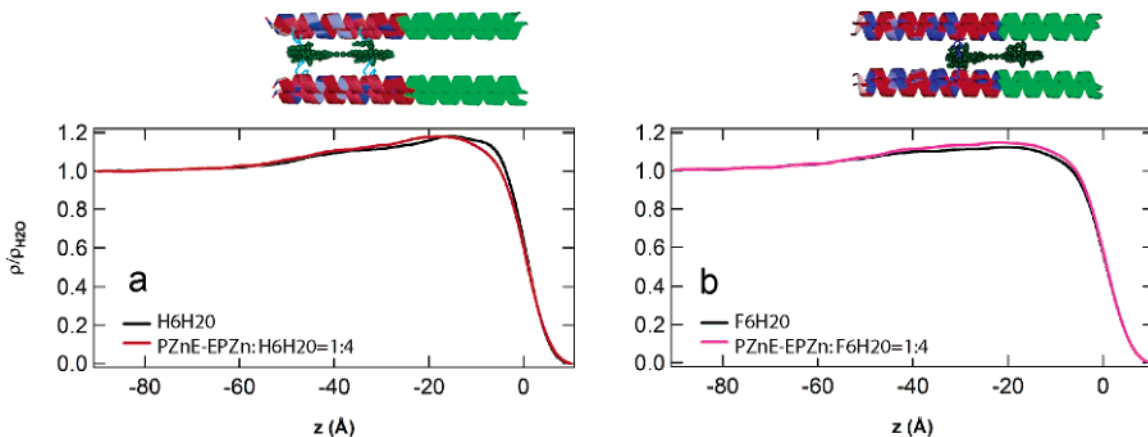
Figure 4. Comparison of the monolayer electron density profiles for the *apo* and *holo* forms of AP0 peptides with 1 PZnE-EPZn bound per 4-helix bundle. (a) The profile structures of *H6*H20 AP0 from Figures 2 and 3 at a constant area of 200 Å²/helix, corresponding to a high surface pressure with a large fraction (>95%) of the helices are oriented perpendicular to the water−air interface enabling this comparison. The electron density is seen to be slightly higher within the hydrophilic domain (−50 Å < z < −20 Å) and slightly lower within the hydrophobic domain (−20 Å < z < 0 Å) of the amphiphilc 4-helix bundle for the *holo* form. (b) The profile structures of the F6H20 variant of AP0, also at constant area of 200 Å²/helix and with a similar degree of orientation of the bundles. The electron density is seen to be slightly higher over a region spanning both the hydrophilic and the hydrophobic domains (−35 Å < z < −5 Å) of the amphiphilic 4-helix bundle for the *holo* form. The molecular graphics representations of the 4-helix bundles juxtaposed above each pair of profile structures show the cofactors in different locations for the two different peptides, consistent with the differences between profile structures of the *apo* and *holo* forms, as well as with the electronic absorption spectra shown in Figure 6.

stoichiometry of 1 cofactor/4-helices, are very similar, as shown in Figures 2 and 3. At higher surface pressures where >90% of the helices are oriented perpendicular to the interface (e.g., for areas/helix ≤ 200 Å²), the interface between the end of the hydrophilic domain of the AP0 peptide and the pure aqueous subphase located at $z \approx -50$ Å is slightly broader, the average electron density within the hydrophilic domain (−50 Å < z < −20 Å) is slightly greater, and the average electron density within the hydrophobic domain (−20 Å < z < 0 Å) is somewhat lower for the *holo* form than for the *apo* form, as shown in Figure 4a. For the PZnE-EPZn cofactor and F6H20 AP0, the electron density profiles for the *apo* and the *holo* forms, at a stoichiometry of 1 cofactor/4-helices, are again very similar, as shown in Figure 5. However, for this variant of AP0 the electron density of the *holo* form is slightly greater than that for the *apo* form over the region −35 Å < z < −5 Å. Consideration of the electronic absorption spectra of the PZnE-EPZn cofactor within the H6H20, H6F20, and F6H20 variants at the same stoichiometry indicates that the cofactor environments, constraining the PZn−PZn interplanar torsional angle distribution as well as the conformeric population-weighted average PZn−PZn torsional angle are similar for the H6H20 and H6F20 variants but different for the F6H20 variant (Figure 6). Because the cofactor can only occur within the hydrophilic domain of the H6F20 variant, the above results, considering both the profiles and the corresponding spectra, suggest that the PZnE-EPZn cofactor is incorporated into the hydrophilic domain of the H6H20 and H6F20 variants and spans the interface between hydrophilic and hydrophobic domains within the F6H20 variant, as shown in Figure 4. For the Ru-PZn²⁺ cofactor and H6H20 AP0, the electron density profiles for the *apo* and the *holo* forms, at a stoichiometry of 1 cofactor/4-helices, are less similar, as shown in Figure 7. The hydrophilic

domain of the α-helical bundle peptide shortens by ~5 Å, and the interface between the hydrophilic domain and the pure aqueous subphase sharpens substantially upon incorporation of the cofactor. The electronic absorption spectra for this cofactor and the H6F20 and F6H20 variants of the AP0 peptide indicate that axial histidyl ligation of the Zn-porphyrin portion of the cofactor occurs only at the H6 site for the dimer (i.e., the dihelical form). Thus, these changes in the monolayer electron density profile arise from incorporation of the Ru-PZn²⁺ cofactor within the hydrophilic domain of the H6H20 variant. Definitive evidence for the precise localization of the PZnE-EPZn and Ru-PZn²⁺ cofactors within the profile structures of these amphiphilic 4-helix bundle peptides will require the utilization of resonance X-ray reflectivity to localize the positions of the cofactor metal atoms with the profile structures.[17]

Grazing-incidence X-ray diffraction (GIXD) data, $I(q_{xy}, q_z)$, from Langmuir monolayers of the amphiphilic H6H20 and F6H20 AP0 peptides in their *apo* and *holo* forms with the PZnE-EPZn cofactor at cofactor/peptide mole ratio of 1−2/4-helix bundle, and the H6H20 AP0 peptide with the Ru-PZn²⁺ cofactor at 1 cofactor/4-helix bundle, at higher surface pressures all show a broad maximum for momentum transfer parallel to the monolayer plane at $q_{xy} \approx 2\pi/11$ Å⁻¹, as shown in Figure 8. This diffraction, which is absent in such data from the aqueous subphase itself and Langmuir monolayers of phospholipids on its surface, arises from the interference between parallel helices, becoming progressively more localized to the neighborhood of the q_{xy} axis with increasing surface pressure as a larger fraction of the helices become oriented perpendicular to the interface. The q_{xy} dependence of this GIXD data for *apo*-H6H20 AP0 (Figure 9) and its inverse Fourier transform, namely, the in-plane radial autocorrelation function, were modeled approximating the helices as straight rods of uniform electron density of
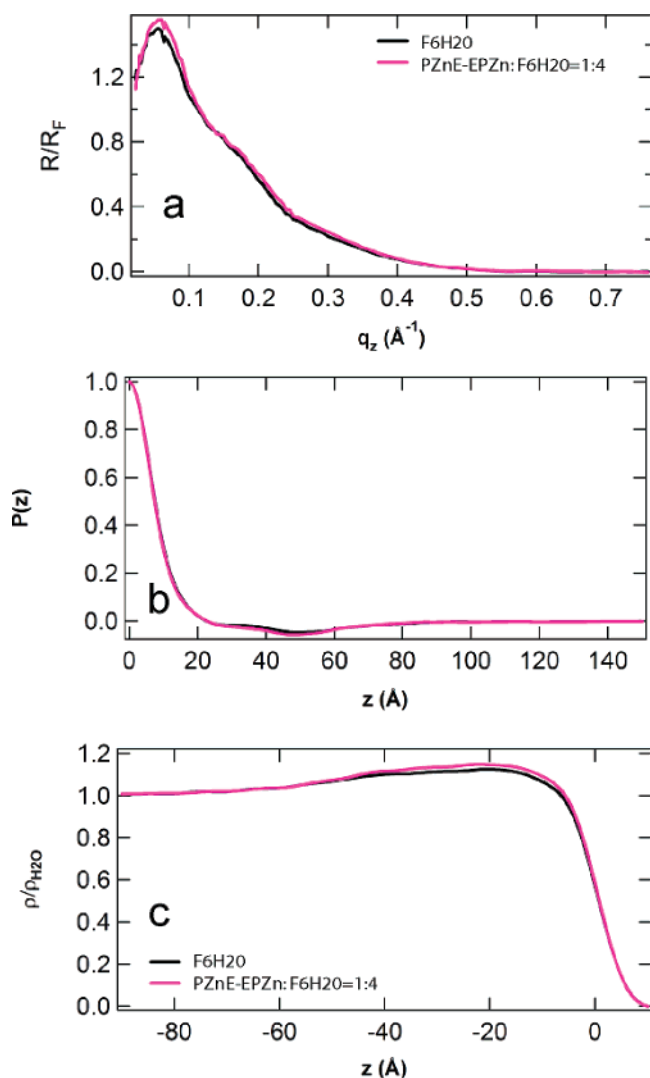
Figure 5. Fresnel-normalized X-ray reflectivity data (a), and the corresponding autocorrelation of the gradient electron density profiles (b) and absolute electron density profiles themselves (c) derived from these data, for Langmuir monolayers of the *apo* form and the *holo* form of the *F*6H20 variant of the AP0 peptide with the PZnE-EPZn cofactor at one cofactor/4-helix bundle at a relatively high applied surface pressure corresponding to 200 Å^2/helix (also shown in Figure 4b). At such high surface pressures, a large fraction (>95%) of the helices are oriented perpendicular to the water−air interface enabling this comparison of the *apo* and *holo* forms. The electron density is seen to be slightly higher over a region spanning both the hydrophilic and the hydrophobic domains (-35 Å $< z < -5$ Å) of the amphiphilic 4-helix bundle for the *holo* form.

$\sim$5−10 Å diameter and using analytical expressions developed by Harget and Krimm.[18] For *apo*-AP0, the modeling demonstrates that the dihelices aggregate to form 4-helix bundles, which are rotationally disordered about the normal to the membrane plane with glass-like interbundle positional ordering in the monolayer plane. Other possible bundles of the AP0 dihelices can be readily excluded on this basis because their respective GIXD and corresponding radial autocorrelation functions differ qualitatively, well outside the signal-to-noise level, from their experimental counterparts. Comparison of the q_{xy} dependence of the model and experimental GIXD, allowing for the finite Δq_{xy} resolution,

provides reasonable agreement for a 4-helix bundle of $\sim$6.0 Å diameter helices at a $\sim$10.5 Å interhelix separation for a square arrangement of the four helices in the plane perpendicular to the bundle axis. A rhombic arrangement of the four helices in the plane perpendicular to the bundle axis of the same $\sim$6.0 Å diameter, but with a $\sim$11.5−11.75 Å interhelix separation, is shown to produce a better fit than a square arrangement for the *apo* form of the H6H20 AP0 peptide; see Figure 10. We note that the relatively small diameter of the best-fitting solid cylinder, that is, 6−6.5 Å as opposed to $\sim$10 Å, is a direct result of the dominance of the α-carbon backbone in the projection of the α helix onto the plane perpendicular to its long axis. The differences in the q_{xy} dependence of this GIXD data for the *apo* versus the *holo* forms of H6H20 AP0 are very similar for both the PZnE-EPZn and Ru-PZn^{2+} cofactors, as shown for the PZnE-EPZn case at 0, 1, and 2 cofactors/4-helix bundle in Figure 9. This difference can be modeled by assuming that the incorporation of either the PZnE-EPZn or the Ru-PZn^{2+} cofactor into the interior of the 4-helix bundle at 1 cofactor/4-helix bundle simply introduces a variation in the interhelix separation over the length of the bundle, noting that both of these cofactors are incorporated into the hydrophilic domain of H6H20 AP0, as described above. Assuming this variation to be random with a symmetric Gaussian distribution of σ width $\sim$1.5 Å about the mean interhelix separation of $\sim$11.5 Å for the rhombic arrangement is seen to be sufficient to explain the changes observed, as shown in Figure 11. Of course, this model is overly simplistic in that the variation would be expected to be systematic, rather than random, over the length of the bundle depending on the location of the cofactor, but the GIXD data being modeled arise from the projection of the bundle onto the plane perpendicular to the bundle long-axis, thus making the model reasonably appropriate for this projection. For the F6H20 variant of AP0, noting that this cofactor is incorporated extending from the hydrophilic into the hydrophobic domain of F6H20 AP0 as described above, incorporation of the PZnE-EPZn cofactor at the same stoichiometry nevertheless has an entirely similar effect on the q_{xy} dependence of this GIXD data for the *apo* versus the *holo* forms.

The q_z dependence of the GIXD data for the *apo* form of the H6H20 AP0 peptide has a primary maximum at $q_z = 0$ Å^{-1} and a weaker secondary maximum for $q_z > 0$ Å^{-1} at $q_z \approx 0.25$ Å^{-1}. The GIXD data can be analyzed in terms of Crick's analysis of the Fourier transform of coiled coil, consistent with the design of AP0 based on the heptad repeat.[19,20] According to this analysis, the pitch, P, of the major helix results in diffraction described as "layer lines" aligned parallel to q_{xy} with a separation along q_z of $2\pi//P$. For a 4-helix bundle, the first observable layer line for $q_z > 0$ Å^{-1} would occur for $\ell = 4$. Assuming the secondary maximum off the q_{xy} axis for $q_z > 0$ Å^{-1} occurring at $q_z \approx 0.25$ Å^{-1} to be this first observable layer line from a coiled coil indicates, for a 4-helix bundle, that the pitch of the major helix, P, is $\sim$100 Å. Using an approximate value of $r \approx 5$ Å for the radius of the major helix results in a pitch angle [given by $\tan^{-1}(2\pi r/P)$] of $\sim$17°. Incorporation via axial
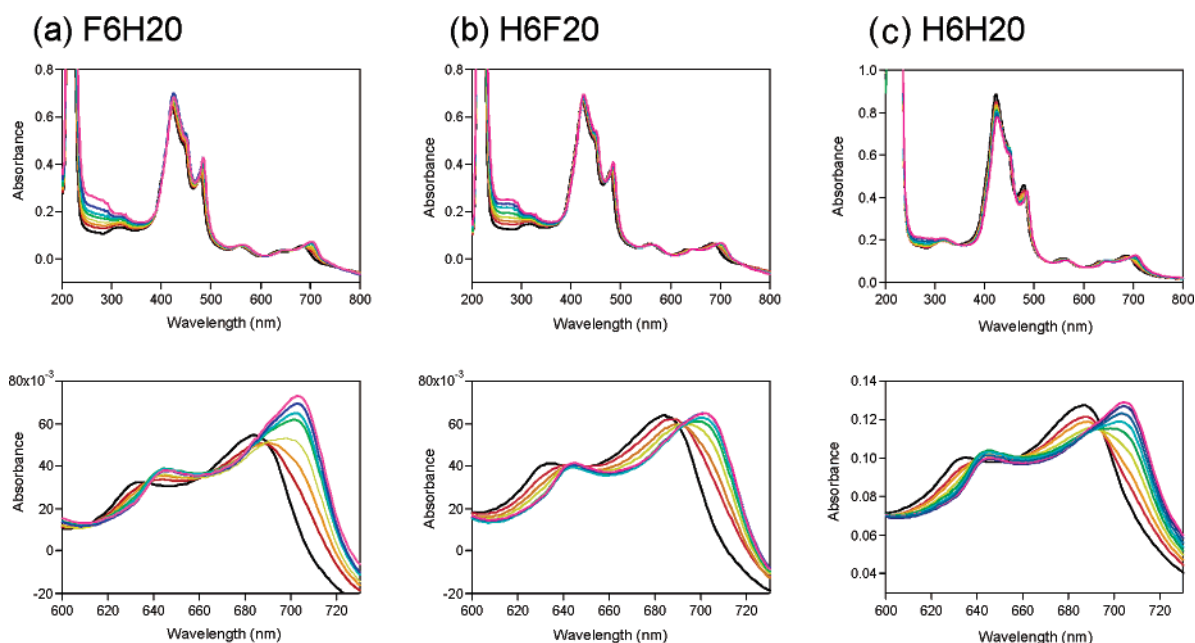
Figure 6. Electronic absorption spectra (upper) and Q-band regions thereof (lower) for the PZnE-EPZn cofactor incorporated into the three variants of the AP0 peptide, H6H20, F6H20, and H6F20, over the range of zero to one 4-helix bundle/cofactor. The red-shifted Q band features upon binding of the cofactor to the peptide via axial histidyl ligation are very similar for the H6F20 and H6H20 variants and different from those exhibited by the F6H20 variant.

histidyl ligation of the much smaller Fe-porphyrin cofactor into the 4-helix bundle F6H20 AP0 tends to remove this signature of the regular coiled-coil structure of the *apo* form, as demonstrated by both the experimental GIXD data and that predicted by molecular dynamics simulations of this system.[21] As a result, this aspect of the GIXD data was not pursued here for the much larger PZnE-EPZn and Ru-PZn^{2+} cofactors.

Polarized absorption/emission spectroscopy was utilized to investigate the orientation of the Zn-porphyrins within the PZnE-EPZn cofactor, incorporated into the interior of the AP0 peptide (for both H6H20 and its variant F6H20) at cofactor/peptide mole ratios of 1/4-helix bundle, relative to the long axis of the helices in Langmuir monolayers of the cofactor/peptide complex as a function of applied surface pressure. Two fluorescence techniques were employed, namely, polarized total internal reflection fluorescence (PTIRF) and polarized epifluorescence (PEF), both measuring fluorescence from the cofactor polarized parallel or perpendicular to the plane of incidence of the excitation as a function of the latter's polarization parallel or perpendicular to the plane of incidence. The PTIRF measurements were performed with an alkylated prism in van der Waals contact with the Langmuir monolayer of the cofactor/peptide complex on the aqueous subphase from above, as well as following deposition of the Langmuir monolayer onto the alkylated prism via "horizontal lift" into the air above the subphase, at the lower and higher pressure extremes for the pressure−area isotherms, for example, 10 and 40 mN/m. The comparatively more simple PEF measurements were performed over the full range of 2−45 mN/m. Data collection and the analysis of such data have been described in detail previously[22] and will not be repeated here; relevant Figures are presented in the Supporting Information.

Combination of these PEF and PTIRF measurements provide sufficient data to determine both the dielectric constant for the cofactor's local environment within the monolayer and the orientational distribution parameters for the (porphinato)zinc macrocycles of the PZnE-EPZn cofactor. The analysis indicates that PZnE-EPZn is almost completely exposed to the aqueous subphase at the lower pressure extreme ($n_f = 1.34 \pm 0.01$ at 10 mN/m) and buried inside the densely packed peptide at the higher pressure extreme ($n_f = 1.51 \pm 0.07$ at 40 mN/m). The larger error in the latter case arises from the larger fraction of peptide relative to solvent in the monolayer at the higher pressure extreme (or "filling factor") coupled with the uncertainty in the peptide's refractive index, assumed to be in the range of 1.48−1.60 (see the Supporting Information for details). In addition, the analysis indicates that mean tilt angle of the PZnE-EPZn (porphinato)zinc planes relative to the monolayer plane (measured as the unique angle between the normal to the porphyrin plane and the normal to the monolayer plane) changed substantially from $33 \pm 3°$ at 10 mN/m to $53 \pm 3°$ at 40 mN/m. The widths of the distribution were relatively narrow, namely, $5 \pm 5°$ and $10 \pm 10°$ at these two extremes of the isotherm, respectively. Furthermore, the PEF measurements indicated that this change occurs as a relatively abrupt transition at 30−35 mN/m. This analysis assumed only that the absorption and emission transition dipoles lie in the plane of the porphyrin ring (see below). The transition in mean orientation of the PZnE-EPZn chromophore can be shown to be independent of the change in its local environment (i.e., the orientational transition occurs even if the refractive index of the chromophore's local environment remained constant through the transition).

Two models (see Figure 12) were explored to reconcile the X-ray scattering data (reflectivity and GIXD) and the
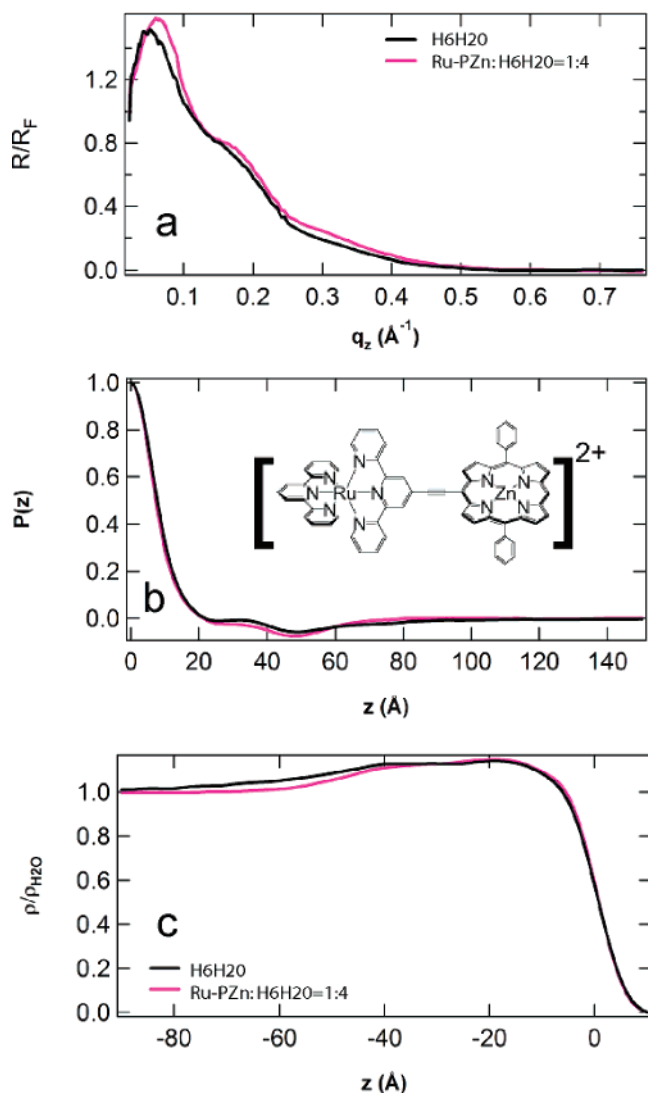
Figure 7. Fresnel-normalized X-ray reflectivity data (a), and the corresponding autocorrelation of the gradient electron density profiles (b) and absolute electron density profiles themselves (c) derived from these data, for Langmuir monolayers of the *apo* form and the *holo* form of the H6H20 variant of the AP0 peptide with the Ru-PZn^{2+} cofactor (inset) at one cofactor/4-helix bundle at a relatively high applied surface pressure corresponding to 200 Å^2/helix. At such high surface pressures, a large fraction (>95%) of the helices are oriented perpendicular to the water−air interface enabling this comparison of the *apo* and *holo* forms. The hydrophilic domain of the α-helical bundle peptide shortens by ∼5 Å, and the interface between the hydrophilic domain and the pure aqueous subphase sharpens substantially upon incorporation of the cofactor, its Zn-porphyrin bound via axial histidyl ligation at H6.

polarized absorption/emission data (PTIRF and PEF) from the Langmuir monolayers of the F6H20 AP0 complex with the PZnE-EPZn cofactor. Such models must also take into account the designed amphipathicity of the helices, which we assume to be dominated by the first four heptads of the six heptad α-helix. The results from the analysis of the X-ray data provide the average orientation of both the long axis of the helices and the plane of the dihelical peptide relative to the plane of the monolayer, whereas analysis of the spectroscopic data provides the average orientation of the Zn-porphyrin plane of the chromophore relative to the plane of

the monolayer. The most simple model allows for only one orientational distribution of the porphyrin chromophores and only one orientational distribution of the helices, each modeled as a single Gaussian described by its mean and σ-width, with respect to the monolayer plane. Such a simple model suffices only at the lower extreme of the pressure−area isotherm, for example, for pressures ≤10−12 mN/m where the helices are not closely packed at the interface with all helices lying in the plane of the interface. This lack of close-packing coupled with the axial histidyl ligation of one Zn-porphyrin of the PZnE-EPZn cofactor to only one of the two helices comprising the dihelix presumably allows for the ∼30° tilt of the porphyrin normal with respect to the normal to the interface. In contrast, such a simple model would require that the mean helix orientation must be tilted substantially with respect to the normal to the plane of the monolayer at the higher surface pressures, namely, ∼35° at the upper extreme of the isotherm for pressures ≥40mN/m, in order to accommodate intercalation of the cofactor's Zn-porphyrins among the close-packed helices, which is not consistent with the X-ray results, namely, both the monolayer electron density profile and the GIXD. However, inspection of the monolayer electron density profiles indicates that the distribution of orientations of the plane of the dihelix relative to the plane of the monolayer becomes progressively more "bimodal", namely, a superposition of two Gaussians, over the midrange of 20−30 mN/m of the isotherm in which the long axis of the helices remain parallel to the plane of the interface. This bimodal distribution then further evolves into a superposition of mean helix orientations both perpendicular and parallel to the interface at the higher pressure extreme, for both the F6H20 and H6H20 versions of the AP0 peptide. Using a bimodal distribution of chromophore orientations, with two mean porphyrin ring orientations both parallel and perpendicular to the plane of the monolayer, brings the polarized spectroscopy results into substantially better agreement with the X-ray results for pressures ≥20 mN/m. For example, over the midrange of the isotherms, where the helices approach and then exceed close-packing in plane of the interface, the relative populations of the chromophore in this best-fit model with their porphyrin rings parallel to the monolayer plane (associated with dihelices with an average orientation of the long axis of the helices parallel to the plane of the monolayer and the plane of the dihelical peptide perpendicular to the plane) and those with their porphyrin rings perpendicular to the monolayer plane (associated with dihelices with an average orientation of the long axis of the helices parallel to the plane of the monolayer and the plane of the dihelical peptide parallel to the plane) would be ∼50 ± 5 and ∼50 ± 5%. At the higher pressure extreme of the isotherm, the relative populations of the chromophore in this best-fit model with their porphyrin rings parallel to the monolayer plane (associated with dihelices with an average orientation of the long axis of the helices parallel to the plane of the monolayer and the plane of the dihelical peptide perpendicular to the plane) and those with their porphyrin rings perpendicular to the monolayer plane (associated with the helices of the dihelical peptide oriented
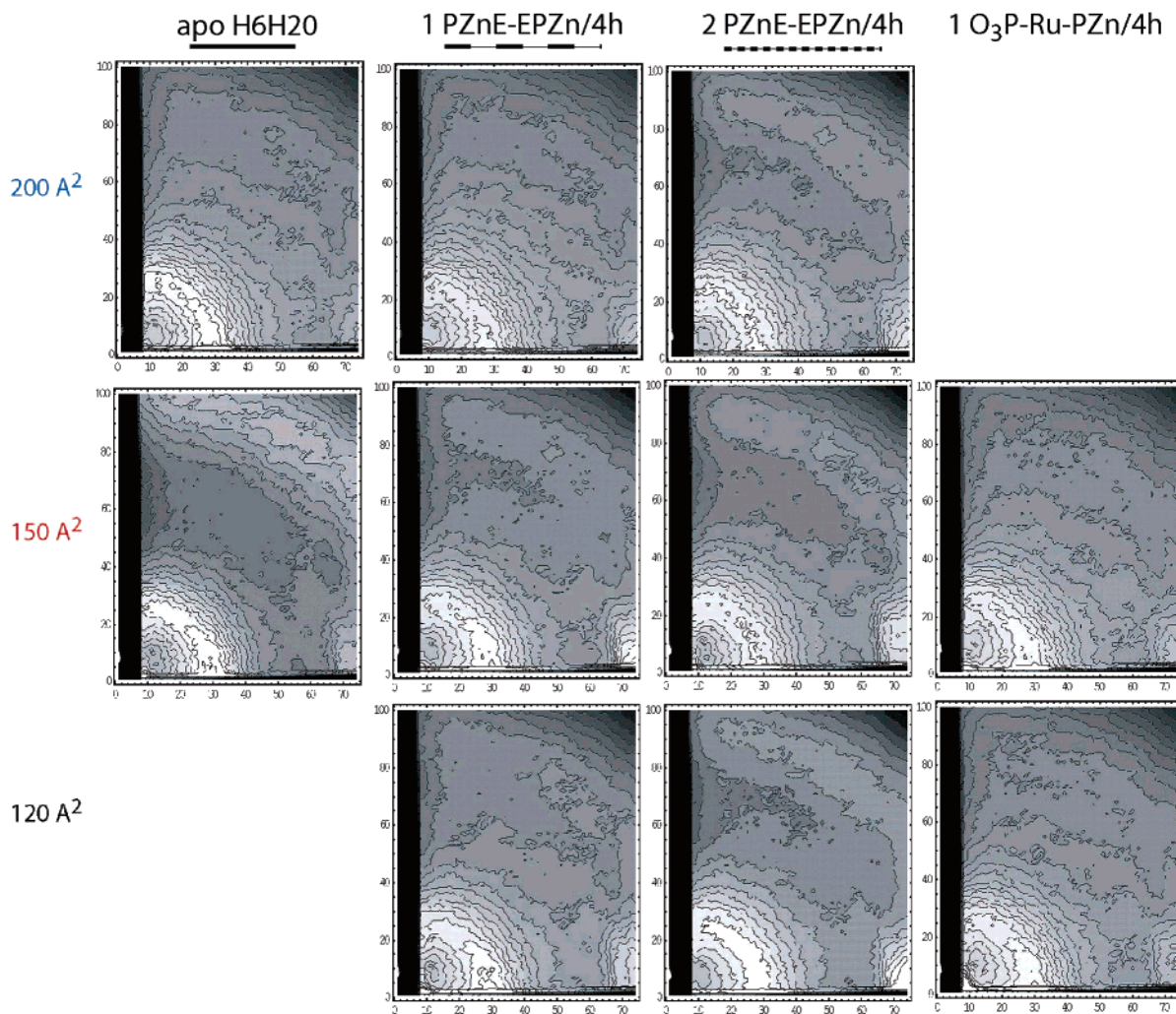
Figure 8. Grazing-incidence X-ray diffraction (GIXD) data shown as contour plots for *apo*-H6H20 AP0 and its *holo* forms with the PZnE-EPZn and O_3P-Ru-PZn cofactors at one and two cofactors/4-helix bundle and at one cofactor/4-helix bundle, respectively. The abscissa in each represents the q_{xy} axis and the ordinate represents the q_z axis, with the indices representing increments of 0.02 Å^{-1}. The interhelix interference from within a bundle, located approximately at index value 30 along the q_{xy} axis, becomes progressively more localized nearer the q_{xy} axis as the average area/helix decreases in the Langmuir monolayer with increasing surface pressure as the fraction of helices oriented more perpendicular to the interface increases. (For the GIXD measurements, we used O_3P-Ru-PZn, a phosphorylated version of Ru-PZn^{2+}. There was no difference in the optical spectra or binding behavior of these two cofactors.)

perpendicular to the plane) would be ~30 ± 3 and ~70 ± 3%. The relative populations of the two mean orientations in these bimodal distributions were found to be uncorrelated with their widths, the latter being ~5° at 40 mN/m. This result for the higher pressure extreme of the isotherm is in reasonably good agreement with that from X-ray reflectivity indicating 20−25% and 75−80%, respectively. For the H6H20 form of AP0, the polarized spectroscopy results were similar to those described above for the F6H20 variant. However, the X-ray scattering results indicate a significantly higher fraction of helices oriented with their long axis normal to the monolayer plane at higher surface pressures (e.g., ~90%), thereby providing only rough agreement with the polarized spectroscopy results. The less-than-perfect agreement described above does not seem particularly surprising, given that the polarized spectroscopy and X-ray scattering measurements could not be performed simultaneously on the same monolayer of the peptide/cofactor complex.

Utilization of a conjugated porphyrin dimer cofactor such as PZnE-EPZn should be particularly interesting for the polarized linear spectroscopy studies because in this case, the axial symmetry is reduced to D_2. This results in two different, mutually perpendicular absorption transition dipoles in the plane of the porphyrin ring, one at slightly higher energy aligned perpendicular (Y) and one at slightly lower energy aligned parallel (X) to the long conjugation axis, with the emission transition dipoles aligned only along the conjugation axis.[9,10,12,14,23,24] Unfortunately, the CW nature of our PEF and PTIRF measurements as currently configured, with emphasis on the polarization dependence of the excitation, thereby precludes their ability to determine the orientation of the conjugation axis of the PZnE-EPZn cofactor relative to the normal to the plane of a monolayer of vectorially oriented cofactor−peptide complexes. Nevertheless, molecular modeling suggests that the long conjugation axis of the cofactor must be aligned within less than 45°
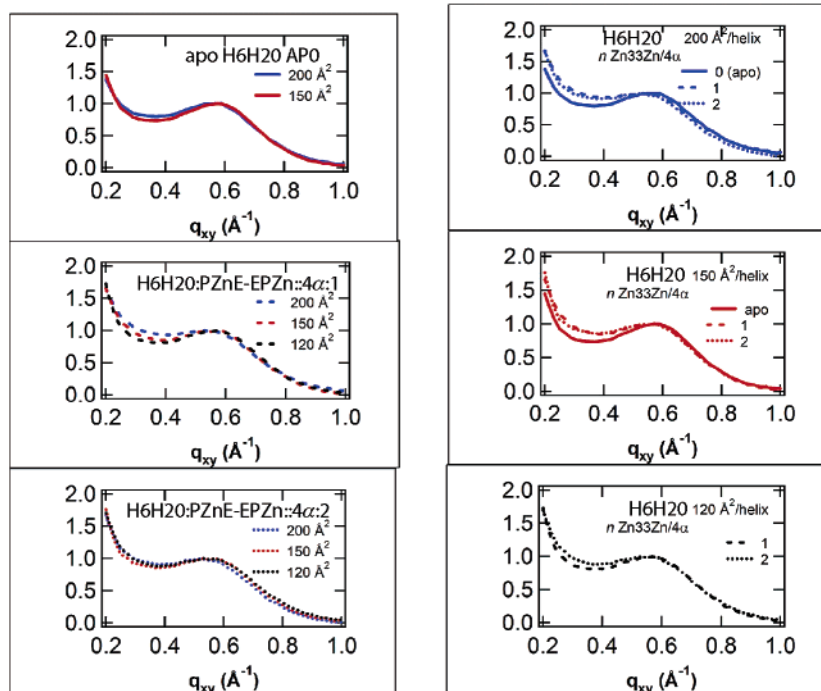
Figure 9. q_{xy} dependence of the GIXD data from Figure 8 for the *apo* and *holo* forms with the PZnE-EPZn cofactor is shown, obtained via integration of the 2-dimensional data over a strip defined by 0 Å^{-1} < q_z < 0.1 Å^{-1}. The interhelix interference maxima at $q_{xy} \approx 0.6$ Å^{-1} becomes more pronounced for each of the *apo* and *holo* forms with decreasing area/helix and the differences between the *apo* and the *holo* forms are seen to be systematic at each of the three areas/helix investigated at the higher applied surface pressures.
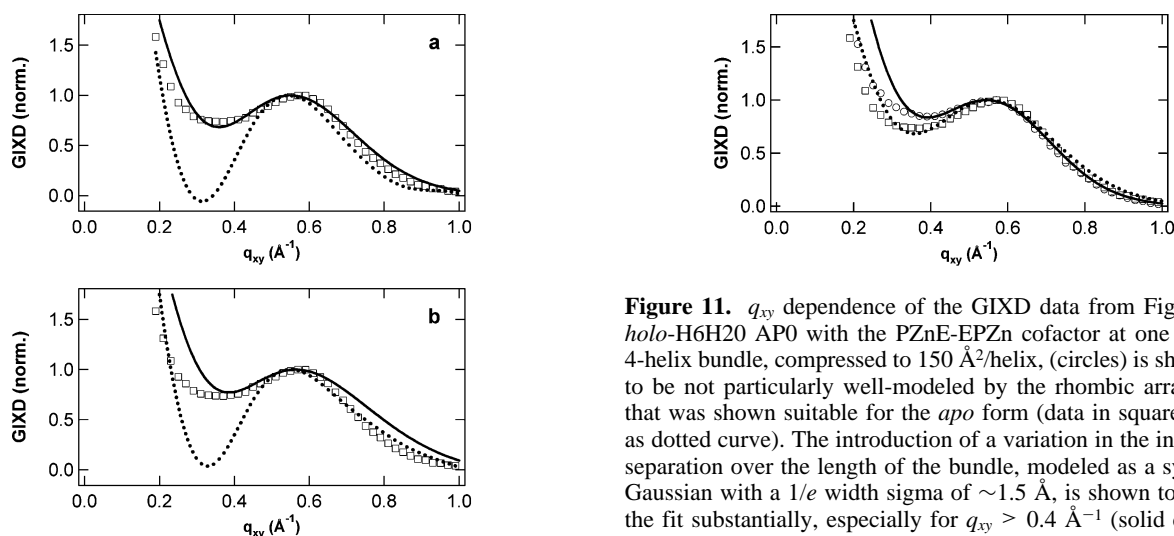
Figure 10. q_{xy} dependence of the GIXD data from Figure 9 for *apo*-H6H20 AP0 at 150 Å^2/helix (squares) is modeled as an aggregate of four solid cylinders representing the helices. A rhombic arrangement of the cylinders in the plane perpendicular to the long axis of the aggregate, i.e., in the plane of the monolayer, is seen to provide a better fit to the data (a) than a square arrangement (b), allowing for the finite Δq_{xy} resolution of the GIXD experiment (the dotted curves show results for the same models when the experimental resolution is not included in the calculation).

with respect to the long axis of the 4-helix bundle for it to be contained entirely within the bundle, consistent with the dielectric constant for its local environment and thereby also allowing for rotational disorder of the cofactor/peptide complex about the normal to the monolayer plane at higher surface pressures consistent with the GIXD.

Figure 11. q_{xy} dependence of the GIXD data from Figure 9 for *holo*-H6H20 AP0 with the PZnE-EPZn cofactor at one cofactor/4-helix bundle, compressed to 150 Å^2/helix, (circles) is shown here to be not particularly well-modeled by the rhombic arrangement that was shown suitable for the *apo* form (data in squares, model as dotted curve). The introduction of a variation in the interhelical separation over the length of the bundle, modeled as a symmetric Gaussian with a 1/e width sigma of ~1.5 Å, is shown to improve the fit substantially, especially for q_{xy} > 0.4 Å^{-1} (solid curve).

In conclusion, these structural studies indicate that the amphiphilic 4-helix bundle AP0 peptide and its variants can effectively vectorially orient extended, conjugated abiological chromophores such as PZnE-EPZn and Ru-PZn^{2+} in cofactor−peptide ensembles on the macroscopic length scale. The vectorial orientation is achieved via the axial histidyl ligation of only one Zn-porphyrin component of the cofactor coupled with the strong amphiphilicity of the bundle. The average stoichiometry of one cofactor per 4-helix bundle results in the large fraction of the vectorially oriented ensemble possessing only one chromophore per bundle, the arrangement of the four helices in the cross section of the bundle being rhombic. Importantly, the disulfide linkage between the two helices forming the dihelices comprising the AP0
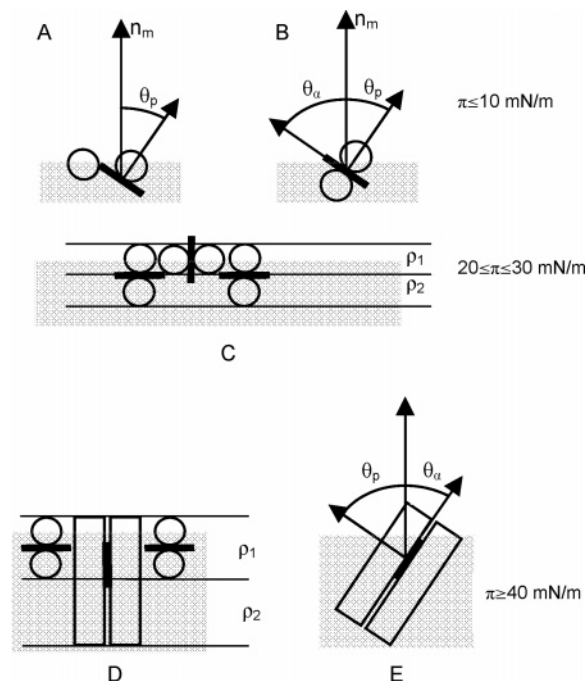
Figure 12. Models for understanding the polarized fluorescence spectroscopy of the *holo* form of AP0 with the PZnE-EPZn cofactor. The two helices of the dimer are shown end-on as empty circles and side-on as empty rectangles, and the Zn-porphyrin is shown edge-on as a solid rectangle. The angle between the normal to the plane of the interface n_p and *a)* the porphyrin plane is θ_α and *b)* the normal to the plane of the porphyrin ring is θ_p. At lower surface pressures (≤ 10 mN/m), the distribution of Zn-porphyrin orientations can be represented by a single Gaussian with a measured mean value for $<\theta_p>$ of ~30° and remain consistent with the long axis of the helices lying parallel to the plane of the interface, with the plane of the dihelices lying parallel (upper left) or near-parallel (upper right) to the interface, as indicated by the monolayer electron density profiles. At higher surface pressures (≥ 40 mN/m), a single Gaussian is insufficient, as a measured mean value for $<\theta_p>$ of ~60° would require that the long axis of the helices be inclined ~60° to the plane of the interface (lower right), which is not consistent with either the monolayer electron density profiles or the GIXD data indicating that the helices are oriented predominately perpendicular to the interface. A "bimodal" distribution, namely, a superposition of two Gaussians, is more consistent with the X-ray scattering results with ~70% of the Zn-porphyrins having a mean value for $<\theta_p>$ of ~90° and ~30% with a mean value for $<\theta_p>$ of ~0° (lower left). Such a "bimodal" distribution is similarly more suitable for the intermediate range of surface pressures (20−30 mN/m) over which the plane of the dihelices rotates from more parallel to more perpendicular to the plane of the interface (middle).

4-helix bundle peptide are exposed on the upper surface of the Langmuir monolayer ensembles of the vectorially oriented cofactor−peptide complex at higher surface pressures. This can be exploited to covalently attach the vectorially oriented ensemble of cofactor−peptide complexes to the planar surface of solid inorganic substrates,[15] as important for potential nonlinear optical device applications, as already demonstrated with closely related peptides. Utilizing this approach, initial studies have already demonstrated highly efficient second harmonic generation (SHG) from single monolayer films of the H6H20 AP0 peptide, covalently attached to an alkylated quartz surface possessing thiol endgroups, only upon the in situ incorporation of the
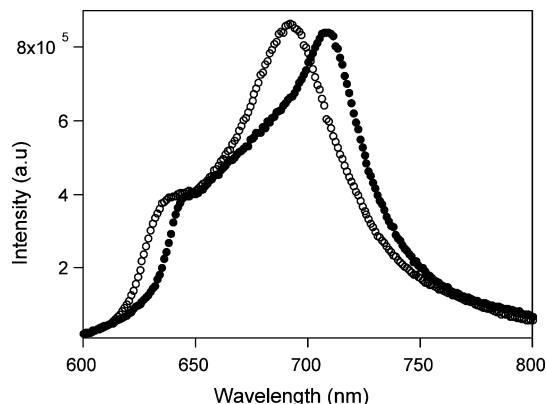

Figure 13. Fluorescence emission spectra for the PZnE-EPZn cofactor (empty circle) are shown to red-shift (solid circle) upon incorporation into the amphiphilic 4-helix bundle peptide AP0.

Ru-PZn^{2+} cofactor.[25] Furthermore, such polarized nonlinear spectroscopic measurements can also provide the average orientation of the cofactor conjugation axis relative to the normal to monolayer plane because the cofactor's hyperpolarizability tensor, β, should be dominated by its component along the conjugation axis.[26]

Supporting Information Available: Experimental details, data analysis, and theoretical calculations on the polarized fluorescence spectroscopy. This material is available free of charge via the Internet at http://pubs.acs.org.

References

(1) Xu, T.; Wu, S. P.; Miloradovic, I.; Therien, M. J.; Blasie, J. K. *Nano. Lett.* **2006**, *6*, 2387.
(2) Ye, S. X.; Strzalka, J. W.; Discher, B. M.; Noy, D.; Zheng, S. Y.; Dutton, P. L.; Blasie, J. K. *Langmuir* **2004**, *20*, 5897.
(3) Ye, S. X.; Discher, B. M.; Strzalka, J.; Xu, T.; Wu, S. P.; Noy, D.; Kuzmenko, I.; Gog, T.; Therien, M. J.; Dutton, P. L.; Blasie, J. K. *Nano Lett.* **2005**, *5*, 1658.
(4) Duncan, T. V.; Rubtsov, I. V.; Uyeda, H. T.; Therien, M. J. *J. Am. Chem. Soc.* **2004**, *126*, 9474.
(5) Uyeda, H. T.; Zhao, Y. X.; Wostyn, K.; Asselberghs, I.; Clays, K.; Persoons, A.; Therien, M. J. *J. Am. Chem. Soc.* **2002**, *124*, 13806.
(6) Anderson, H. L. *Inorg. Chem.* **1994**, *33*, 972.
(7) Arnold, D. P.; Heath, G. A.; James, D. A. *J. Porphyrins Phthalocyanines* **1999**, *3*, 5.
(8) Beljonne, D.; O'Keefe, G. E.; Hamer, P. J.; Friend, R. H.; Anderson, H. L.; Bredas, J. L. *J. Chem. Phys.* **1997**, *106*, 9439.

(9) Lin, V. S. Y.; Dimagno, S. G.; Therien, M. J. *Science* **1994**, *264*, 1105.

(10) Rubtsov, I. V.; Susumu, K.; Rubtsov, G. I.; Therien, M. J. *J. Am. Chem. Soc.* **2003**, *125*, 2687.

(11) Screen, T. E. O.; Thorne, J. R. G.; Denning, R. G.; Bucknell, D. G.; Anderson, H. L. *J. Am. Chem. Soc.* **2002**, *124*, 9712.

(12) Shediac, R.; Gray, M. H. B.; Uyeda, H. T.; Johnson, R. C.; Hupp, J. T.; Angiolillo, P. J.; Therien, M. J. *J. Am. Chem. Soc.* **2000**, *122*, 7017.

(13) Susumu, K.; Duncan, T. V.; Therien, M. J. *J. Am. Chem. Soc.* **2005**, *127*, 5186.

(14) Susumu, K.; Therien, M. J. *J. Am. Chem. Soc.* **2002**, *124*, 8550.

(15) Churbanova, I. Y.; Tronin, A.; Strzalka, J.; Gog, T.; Kuzmenko, I.; Johansson, J. S.; Blasie, J. K. *Biophys. J.* **2006**, *90*, 3255.

(16) Blasie, J. K.; Zheng, S.; Strzalka, J. *Phys. Rev. B* **2003**, *67*, 224201.

(17) Strzalka, J.; DiMasi, E.; Kuzmenko, I.; Gog, T.; Blasie, J. K. *Phys. Rev. E* **2004**, *70*, 051603.

(18) Harget, P. J.; Krimm, S. *Acta Crystallogr., Sect. A* **1971**, *27*, 586.

(19) Crick, F. H. C. *Acta Crystallogr.* **1953**, *6*, 685.

(20) Crick, F. H. C. *Acta Crystallogr.* **1953**, *6*, 689.

(21) Zou, H.; Strzalka, J.; Xu, T.; Blasie, J. K. *J. Phys. Chem. B*, submitted for publication, 2006.

(22) Tronin, A.; Xu, T.; Blasie, J. K. *Langmuir* **2005**, *21*, 7760.

(23) Duncan, T. V.; Susumu, K.; Sinks, L. E.; Therien, M. J. *J. Am. Chem. Soc.* **2006**, *128*, 9000.

(24) Lin, V. S. Y.; Therien, M. J. *Chem.—Eur. J.* **1995**, *1*, 645.

(25) Gonella, G.; Tronin, A.; Xu, T.; Fry, C.; Therien, M. J.; Dai, H.-L.; Blasie, J. K. Unpublished results, 2006.

(26) Karki, L.; Vance, F. W.; Hupp, J. T.; LeCours, S. M.; Therien, M. J. *J. Am. Chem. Soc.* **1998**, *120*, 2606.